Journal of The Electrochemical Society

The Electrochemical Society
Advancing solid state & electrochemical science & technology

OPEN ACCESS

Understanding the Overlithiation Properties of $LiNi_{0.6}Mn_{0.2}Co_{0.2}O_2$ Using Electrochemistry and Depth-Resolved X-ray Absorption Spectroscopy

To cite this article: Camille Usubelli *et al* 2020 *J. Electrochem. Soc.* **167** 080514

Journal of The Electrochemical Society, 2020 **167** 080514

Understanding the Overlithiation Properties of $LiNi_{0.6}Mn_{0.2}Co_{0.2}O_2$ Using Electrochemistry and Depth-Resolved X-ray Absorption Spectroscopy

Camille Usubelli,[1,2,*] Münir M. Besli,[1,3,*] Saravanan Kuppan,[1] Nannan Jiang,[1] Michael Metzger,[1] Aziz Dinia,[2] Jake Christensen,[1,] and Yelena Gorlin[**,z]**

[1]*Robert Bosch LLC, Research and Technology Center, Sunnyvale, California 94085, United States of America*
[2]*Institute of Physics and Chemistry of Materials of Strasbourg (IPCMS), UMR 7504 CNRS, University of Strasbourg, F-67034 Strasbourg Cedex 2, France*
[3]*Dept. of Mech. Engineering, Karlsruhe Institute of Technology (KIT), Karlsruhe 76131, Germany*

One known drawback of Ni-containing layered cathodes is their poor first cycle efficiency of 85%–90%, upon cycling in a practical potential window. The poor first cycle efficiency is likely a result of surface overlithiation due to significant lithium ion diffusion limitation at this bulk state of charge, but the overlithiation properties of Ni-containing cathodes are currently insufficiently understood. This work focuses on one Ni-containing cathode, $Li_xNi_{0.6}Mn_{0.2}Co_{0.2}O_2$, and performs detailed characterization of its intercalation properties both in the poor cycling efficiency region as well as in the overlithiation region, where the bulk lithium ion content rises above the value of 1. The results of the study first demonstrate that it is possible to recover the capacity this cathode "loses" in the first cycle by lowering the applied potential. Then, they establish the possibility to overlithiate $Li_xNi_{0.6}Mn_{0.2}Co_{0.2}O_2$ cathodes by as much as 300 $mAhg^{-1}$ relative to the pristine electrode. Through complementary characterization using ex situ X-ray diffraction and X-ray absorption spectroscopy both the structural changes and the oxidation state variations in the material throughout the overlithiation process are elucidated. The generated knowledge can be used in developing more accurate physics-based models of industrially-relevant batteries.

 [DOI: 10.1149/1945-7111/ab8a9d]

Manuscript submitted January 30, 2020; revised manuscript received April 4, 2020. Published April 27, 2020.

Supplementary material for this article is available online

Lithium ion batteries (LIBs) have a wide variety of applications from portable power electronics to electric vehicles (EV). The current omnipresence of LIBs in the society has encouraged significant research activity on the optimization of the materials from which their main components, the cathode and anode electrodes, are made. The ideal cathode material should combine high reversible capacity and high energy density with a long lifetime and fulfilment of the safety and cost standards.[1,2] Several transition metal (TM) oxides have been investigated as cathodes in the past, and $LiCoO_2$ (LCO) has emerged as one of the most widely used materials in LIBs for portable electronics. It has a high theoretical capacity of 274 $mAhg^{-1}$ and a current practical capacity of approximately 140 $mAhg^{-1}$,[3,4] but due to high cost and high toxicity of cobalt,[5] other materials are also being considered for use as cathodes in LIBs. The high discharge capacity and lower cost of $LiNiO_2$ have made this material an attractive candidate for cathodes for EV applications. However, its synthesis difficulties and instability due to cation mixing between lithium and nickel sites prevent it from being implemented as a standalone material.[6,7] Substituting nickel with cobalt, manganese, or aluminum is a promising way of improving the stability of the material and thus enabling its use in LIBs.[8] As a result, layered $LiMO_2$ (M=Ni, Mn, Co, Al) such as $LiNi_{0.80}Co_{0.15}Al_{0.05}O_2$ (NCA) and $LiNi_aMn_bCo_cO_2$ (NMC, a + b + c = 1) materials, with theoretical capacities of about 280 $mAhg^{-1}$, have been extensively studied and adopted for use in EV applications.[9–14] Nickel-rich NMC (with a > b, c) cathode materials, in particular, have become great candidates to meet the characteristics of an ideal cathode, as they have reduced cost and toxicity, while delivering high practical capacities.[15–19]

Under standard cycling conditions (potential window between 2.8–3.0 V and 4.3–4.5 V),[15,20,21] the first cycle deintercalation capacity delivered by NMCs at a C-rate of C/10 increases with increasing nickel content, with $Li_xNi_{0.33}Mn_{0.33}Co_{0.33}O_2$ (NMC111) delivering 160 $mAhg^{-1}$ and $Li_xNi_{0.8}Mn_{0.1}Co_{0.1}O_2$ (NMC811) delivering 200 $mAhg^{-1}$,[15,21] while the 1st cycle capacity loss typically varies between 85%–90%.[33,37] Although several reports have linked the 1st cycle capacity loss to diffusion limitations due to formation of surface Li_2MO_2 phase,[2,32,34] no detailed investigations exist of overlithiation properties of NMC cathodes. To address the existing lack of understanding of overlithiation properties of these industrially-relevant cathodes, our study focuses on $Li_xNi_{0.6}Mn_{0.2}Co_{0.2}O_2$ (NMC622), an NMC with an intermediate nickel content. In the practical potential window, it is known that the intercalation/deintercalation of lithium ion into NMC622 cathode corresponds to significant changes in the oxidation state of nickel, small variations in the oxidation state of cobalt, and negligible changes in the oxidation state of manganese,[16] but it is not yet known how the valence of these transition metal oxides changes as Li_2MO_2 phase begins to form.

Through detailed investigation of the overlithiation properties of $Li_xNi_{0.6}Mn_{0.2}Co_{0.2}O_2$, we first demonstrate that it is possible to cycle $Li_xNi_{0.6}Mn_{0.2}Co_{0.2}O_2$ to lithium ion content of 1 by lowering the applied potential to 1.65 V. Then, by further lowering the potential to 0.8 V, we demonstrate that $Li_xNi_{0.6}Mn_{0.2}Co_{0.2}O_2$ can access more than 500 $mAhg^{-1}$ of gravimetric capacity, which suggests that it can accommodate a bulk lithium ion content of ~2. Electrochemical characterization is followed by ex situ X-ray diffraction (XRD) and depth-resolved X-ray absorption spectroscopy (XAS) experiments to understand the structural and oxidation state changes associated with the demonstrated high state of overlithiation. XRD results reveal a close to full conversion of $Li_xNi_{0.6}Mn_{0.2}Co_{0.2}O_2$ to Li_2MO_2 phase, while XAS results identify a reduction in the oxidation states of all three TMs relative to the pristine electrode. The identified information on Li_2MO_2 phase can be used in developing more accurate physics-based models, which in addition to tracking the bulk SOC state, incorporate surface states of electrodes during battery operation, thus allowing for more accurate

*Electrochemical Society Student Member.
**Electrochemical Society Member.
[z]E-mail: yelena.gorlin@gmail.com

power and energy predictions. Future work will explore how Ni-content and repeated cycling influences the overlithiation properties of cathodes in the NMC family.

Experimental

Electrochemical measurements.—Electrochemical measurements were performed in a 2032 coin cell (Hohsen, Japan) setup as well as in an ECC-PAT-Core El-Cell (El-Cell, Germany) setup assembled inside an argon-filled glove box (MBraun, Germany; <1 ppm H_2O and <1 ppm O_2). The positive electrodes used in this study were produced at the U.S. Department of Energy's (DOE) CAMP (Cell Analysis, Modeling and Prototyping) Facility, Argonne National Laboratory and consisted of 90 wt% $LiNi_{0.6}Mn_{0.2}Co_{0.2}O_2$ (NMC622) (ECOPRO, Korea), 5 wt% C45 (Timcal/Imerys Graphite & Carbon, Switzerland), 5 wt% 5130 PVDF (Solvay, Belgium) with a loading of 10.03 mg.cm^{-2}; 90 wt% $LiNi_{0.5}Mn_{0.3}Co_{0.2}O_2$ (NMC532) (Toda, USA), 5 wt% C45 (Timcal/Imerys Graphite & Carbon, Switzerland), 5 wt% 5130 PVDF (Solvay, Belgium) with a loading of 11.40 mg.cm^{-2} and 90 wt% $LiNi_{0.8}Mn_{0.1}Co_{0.1}O_2$ (NMC811) (Targray, Canada), 5 wt% C45 (Timcal/Imerys Graphite & Carbon, Switzerland), 5 wt% 5130 PVDF (Solvay, Belgium) with a loading of 9.12 mg.cm^{-2}.

The electrodes were prepared using 14 mm diameter punch (Hohsen, Japan) and brought into the glove box after drying overnight at 120 °C under dynamic vacuum. A 15 mm disk of lithium metal foil (99.9% purity, 500 μm, Rockwood lithium, USA) was used as the anode. Anode and cathode were separated by two layers of Celgard 2325 (Celgard, USA) with a diameter of 18 mm, which were wetted using 30–33 μl of electrolyte. Electrolyte consisted of 1 M $LiPF_6$ dissolved in a 50:50 mixture (by weight) of ethylene carbonate (EC) and diethyl carbonate (DEC) (Gotion, USA). Two spacers, both with a diameter of 15.5 mm and a respective thickness of 1 mm and 0.5 mm (Hohsen, Japan), were added to the coin cell for compression. In the El-Cell, the same electrodes were used as in the coin cell. The anode was placed at the bottom of the El-cell and separated from the cathode using one layer of Celgard 2325 and one 260 μm thick glass fiber separator (ECC1-01-0012-D/L; El-Cell, Germany), with the glass fiber separator coming into contact with the cathode. 100 μl of the electrolyte (1 M $LiPF_6$ in EC:DEC, 50:50 by weight) was added to each El-cell.

The assembled cells were connected to a battery tester (Arbin, USA) and cycled in a temperature chamber (TestEquity, USA) at 25 °C. The cells were left at OCV for 6–10 h to allow sufficient wetting. The current for the lithiation and delithiation of the cells was set to a C-rate of C/10 based on about 80% of the theoretical capacity of 276.5 mAhg^{-1} (1C = 212 mAhg^{-1}). The cells were cycled to an upper cut-off potential of 4.4 V and discharged to different capacity-determined points. Data was collected every 30 s or 3 mV. During data processing, a correction factor ($<$1E-5 A) was applied to intercalation/deintercalation curves in order to account for the current bias of each Arbin cycling channel. Electrochemical results shown in this study are consistent with data from at least two sets of cells for each measurement; one cell is shown in this report.

Physical and chemical characterization of the electrode.—The cathodes used for the physical and chemical characterization were harvested from El-Cells, soaked in diethyl carbonate (DEC) (BASF, Germany) for about 2 h and dried overnight under vacuum. The morphology of the particles was determined using scanning electron microscopy (SEM; JEOL JSM7200F, Japan). The images were obtained using a secondary electron detector, a beam current of 10 A and a voltage of 5 kV. The crystal structure of the samples was studied using X-ray diffraction (XRD) with Cu Kα radiation on a Bruker D8 ADVANCE diffractometer (Bruker, USA). The scans were collected from 10° to 70° (2Θ) at a step size of 0.05 and a rate of 3 seconds per step.

The X-ray absorption spectroscopy (XAS) measurements were performed at the Stanford Synchrotron Radiation Lightsource (SSRL). Ni, Mn, and Co L-edge were probed at the beamline 8–2 under ultrahigh vacuum (10^{-9} Torr) in a single aluminum sample holder at room temperature using a ring current of 500 mA, a 1100 lines per mm spherical grating monochromator, and a spot size of 1 × 1 mm. Cathode samples were attached to an aluminum sample holder via conductive carbon tape in an argon-filled glove box (MBraun, Germany; <1 ppm H_2O and <1 ppm O_2). The prepared aluminum holder was then packed into pouch bags and double sealed inside the glove box prior to transport to the experimental beam line station. Transfer of the samples into the ultrahigh vacuum chamber was done with the help of a glove bag filled with argon to minimize their exposure to air. Both total electron yield (TEY) and fluorescence yield (FY) data were acquired in a single load. The baseline of the L-edge data was subtracted and the area normalized with the

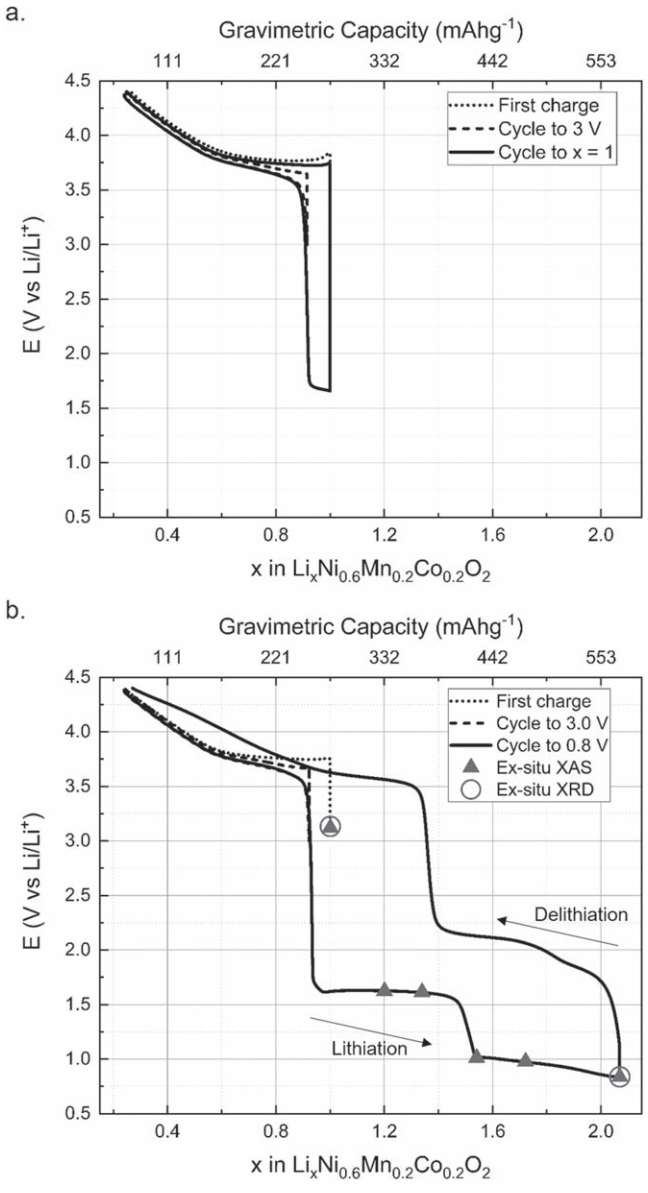

Figure 1. Intercalation/deintercalation profile of $Li_xNi_{0.6}Mn_{0.2}Co_{0.2}O_2$, 1 M $LiPF_6$ in EC-DEC 50:50 half-cells cycled at 0.1 C (a) First delithiation to 4.4 V, intercalation/deintercalation cycle between 4.4 V and 3.0 V, and intercalation/deintercalation cycle to match the initial capacity of xLi = 1 (4.4 V to ~1.65 V); (b) Cell cycled to 0.8 V after a first charge to 4.4 V and one intercalation/deintercalation cycle between 4.4 V and 3.0 V; the triangular and circular shaped markers indicate the capacity and potential at which the different cells were brought and harvested for ex situ hard and soft XAS or XRD measurements.

PyMca software[25] within the range of 633–645 eV for Mn, 771–800 eV for Co and 845–875 eV for Ni.

Hard XAS data for the TMs K-edge of Ni and Co were collected in transmission mode at the beam line 2–2 using a Si (220) monochromator detuned by 40% to reject higher harmonics. Mn K-edge data was collected in transmission mode at beam line 4-3 using a Si (111) monochromator with a 10% detune. Energy calibration was carried out by using the first inflection point of the spectrum of the TM foils as a reference (Ni K-edge = 8332.8 eV, Co K-edge = 7708.9 eV, and Mn K-edge = 6539.0 eV). An absolute energy shift was applied to all Mn spectra, so that the Mn^{4+} edge of the pristine material matched the Mn^{4+} edge of MnO_2 in Manceau et al.[26] The step size for measurements was 0.2 eV in the region of interest and a spot size of 1 × 8 mm was used. X-ray absorption near-edge structure (XANES) data were analyzed and normalized using SIXPACK XAS package,[27] with the photoelectron energy origin (E_0) determined by the first inflection point of the absorption edge jump.

Results and Discussion

Electrochemical cycling of $Li_xNi_{0.6}Mn_{0.2}Co_{0.2}O_2$ ($0.25 < x < 2.06$).—We begin electrochemical characterization of NMC622 electrode by examining a well-recognized feature of nickel-containing cathode materials—the first cycle capacity loss.[15,28–30] We do so by characterizing the electrode at a C-rate of C/10 (21.2 mAg^{-1}) both in a conventional 3.0 V to 4.4 V window and also by decreasing the lower cut-off potential to 1.65 V. The lithium content x in $Li_xNi_{0.6}Mn_{0.2}Co_{0.2}O_2$ is calculated by coulomb counting, assuming that the pristine electrode is fully lithiated. As seen in Fig. 1a, upon the first delithiation from the open circuit potential (OCV) to 4.4 V, the electrode delivers a capacity of 209 $mAhg^{-1}$. During relithiation to 3.0 V, the electrode recovers 183 $mAhg^{-1}$, which corresponds to a first-cycle coulombic efficiency (CE) of 87%. As shown in Table I, our 1st cycle efficiency of 87% at the studied C-rate of C/10 is slightly lower than the value previously observed for NMC622 by Arumugam et al.[28] at a C-rate of C/20 and in line with the efficiencies seen for other Ni-containing cathodes for similar cycling rates. Lowering the cut-off potential from 3.0 V to 1.65 V allows for a complete recovery of the initial capacity of 209.0 $mAhg^{-1}$, bringing CE to 100%. The observed necessity to decrease the lower cutoff potential to recover the lost capacity without reducing the applied current is also consistent with a previous study focusing on $LiNiO_2$.[23] Furthermore, several other publications, which have characterized the 1st cycle capacity loss of Ni-containing electrodes including $LiNi_{1-y}Fe_yO_2$, $LiNi_{0.33}Co_{0.33}Mn_{0.33}O_2$, $LiNi_{0.5}Mn_{0.3}Co_{0.2}O_2$, and $LiNi_{0.80}Co_{0.15}Al_{0.05}O_2$, have shown that the potential needed to recover the first cycle capacity loss is C-rate dependent and can vary from 3.0 V to 1.0 V, depending on the magnitude of the applied current and the type of the cathode material.[24,31–34]

Recovery of the first cycle capacity loss by decreasing the lower cut-off potential to below 2.0 V, as was done in Fig. 1a with a NMC622 electrode, is thought to lead to formation of overlithiated Li_2MO_2 phase on the surface of the particles.[37] For $LiNiO_2$ and $LiMn_{0.5}Ni_{0.5}O_2$ cathodes, it has also been demonstrated that it is possible to extend the formation of Li_2MO_2 phase beyond the surface and into the bulk of the particles for at least one cycle.[22] To determine if a cathode from NMC family is also capable of forming bulk Li_2MO_2 phase, we lowered the cut-off potential of a NMC622 electrode until enough coulombs could be passed to reach a lithium ion stoichiometry of ~2. Figure 1b shows the resulting intercalation/deintercalation profile of a NMC622 electrode, after it was characterized between 4.4 V and 0.8 V. The extended cycle allows to access an additional 294.1 $mAhg^{-1}$ of gravimetric capacity, which corresponds to x = 2.06 in $Li_xNi_{0.6}Mn_{0.2}Co_{0.2}O_2$ (see assumptions and calculation in Table SI is available online at stacks.iop.org/JES/167/080514/mmedia).

We note that the decrease in the lower cut-off potential to 0.8 V introduces interesting features to the intercalation/deintercalation curves. Specifically, two clear plateaus are observed during the overlithiation process, at approximately 1.6 V and 1.0 V, and a third plateau is initiated at approximately 0.8 V. These plateaus are expected to correspond to two-phase transitions and be associated with oxidation state changes in the TMs.[38] It is important to notice that the deep lithiation of the electrode to 0.8 V introduces a small irreversible change, as a capacity of 8.5 $mAhg^{-1}$ (1.7% of the theoretical capacity for insertion of x = 2.06) is not recovered upon deintercalation from 0.8 V to 4.4 V.

Ex situ characterizations.—To link the observed electrochemical features to specific changes in the structure of the material and the oxidation states of the TMs, we carry out a series of ex situ characterization experiments. Using scanning electron microscopy (SEM), we determine that the electrode is about 38 μm thick (Fig. 2a) and examine both the secondary and primary particles in the electrode coating. We find that the secondary particles have a spherical shape and diameter of about 7 to 10 μm (Fig. 2b), while the primary particles have a diameter of about 0.7 to 0.8 μm (Fig. 2c). Due to the use of a slow cycling rate of C/10 in the electrochemical experiments, no electrolyte polarization is expected to occur, and the electrochemical signal is expected to come from the entire thickness of the electrode (Fig. 3a). However, the redox processes at 1.6 V, 1.0 V, and 0.8 V plateaus are likely to begin at the surfaces of the particles, resulting in a gradient within each individual particle throughout the electrode film. Therefore, to properly interpret the measured electrochemical signal, we further rely on a combination of bulk-sensitive and surface-sensitive X-ray techniques.

First, XRD measurements are carried out to identify the structural changes in the bulk of NMC622 electrode (Fig. 3a). Figure 4 presents the XRD patterns of the pristine electrode and the electrode lithiated to 0.8 V. All reflections in the XRD pattern of the pristine

Table I. First Cycle Capacity Efficiency and Recovery of Different Cathode Materials.

Cathode type	1st cycle CE (to 3.0 V)	Recovery	References
$LiNiO_2$	92% @ C/40	~2.0 V	Dahn 1990[23]
$LiNi_{1-y}Fe_yO_2$	83% @ C/50	~1.9 V	Mueller-Neuhaus 2000[31]
$LiNi_{0.33}Co_{0.33}Mn_{0.33}O_2$	89% @ 8 mA g^{-1}	1.47 V	Kang 2008[34]
$LiNi_{0.4}Mn_{0.4}Co_{0.2}O_2$	82% @ C/20	Not studied	Li 2015[35]
$LiNi_{0.5}Mn_{0.3}Co_{0.2}O_2$	89% @ C/50	Hold at 3.0 V	Weber 2017[33]
$LiNi_{0.6}Mn_{0.2}Co_{0.2}O_2$	90% @ C/20	Not studied	Arumugam 2016[28]
$LiNi_{0.6}Mn_{0.2}Co_{0.2}O_2$	87% @ C/10	1.65 V	This work
$LiNi_{0.8}Mn_{0.1}Co_{0.1}O_2$	91% @C/20	Not studied	Li 2015[36]
$LiNi_{0.8}Co_{0.15}Al_{0.05}O_2$	87% @ 8 mA g^{-1}	1.81 V	Kang 2008[34]
$LiCoO_2$	98% @ 8 mA g^{-1}	1.17 V	Kang 2008[34]

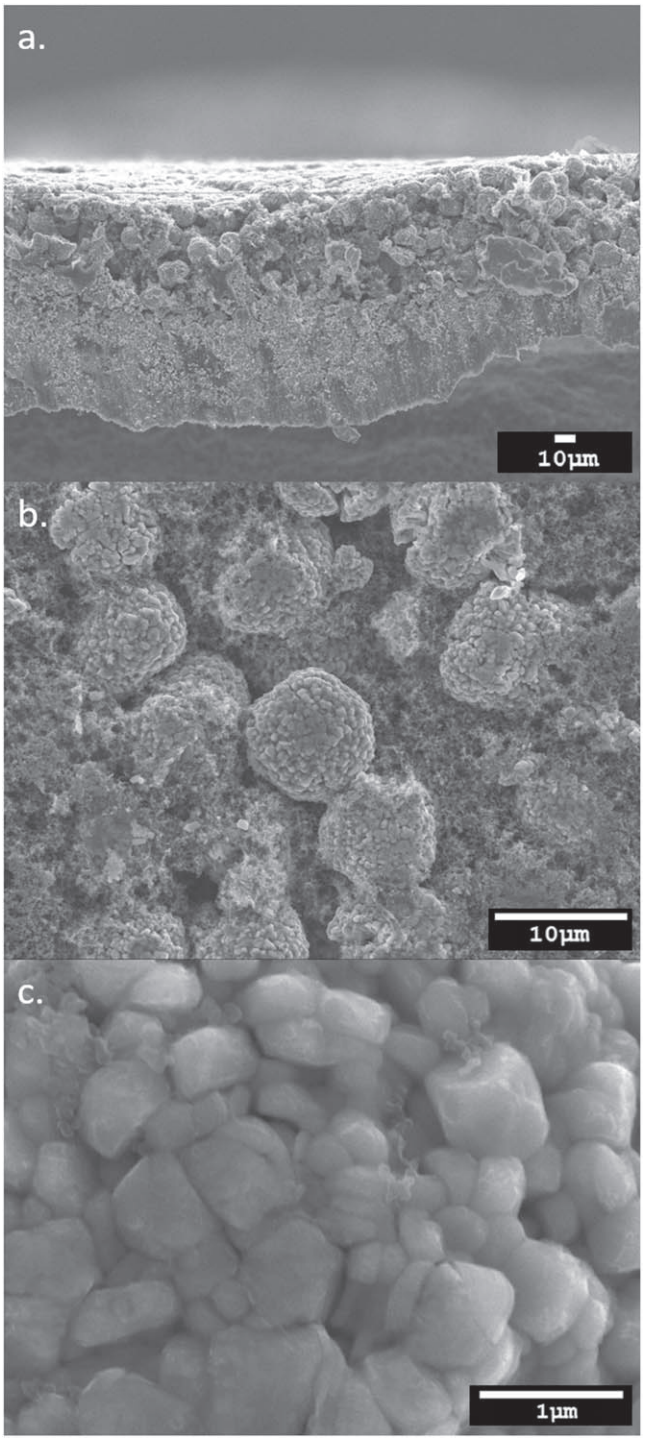

Figure 2. (a) Cross-sectional SEM image of pristine $LiNi_{0.6}Mn_{0.2}Co_{0.2}O_2$ electrode coated on an aluminum film; (b) SEM image of pristine $LiNi_{0.6}Mn_{0.2}Co_{0.2}O_2$ secondary particles of spherical shape and diameter between 7 and 10 μm; (c) SEM image of pristine $LiNi_{0.6}Mn_{0.2}Co_{0.2}O_2$ primary particles of spherical shape and a diameter between 0.7 and 0.8 μm.

material are isostructural with α-$NaFeO_2$, falling into the $R\bar{3}m$ space group.[16,29,39] The major peaks of the XRD pattern of the deeply overlithiated electrode correspond to a material that is isostructural with the 1T-Li_2NiO_2 phase, which was first reported by Dahn et al.,[23] and thus provide support that the overlithiation of the material proceeds via the addition reaction described by Benedek et al.[40] The minor peaks, marked by a star, correspond to particles with the original α-$NaFeO_2$ structure. The lack of full conversion of the electrode to the 1T-Li_2NiO_2 phase suggests that some of the electrochemical features observed in Fig. 1b correspond to side reactions or disconnected particles not participating in the overlithiation of NMC622. We note that although in the conventional cycling window primarily nickel has been shown to participate in the electrochemical redox processes,[16] close to full conversion of $Li_xNi_{0.6}Mn_{0.2}Co_{0.2}O_2$ to $Li_2Ni_{0.6}Mn_{0.2}Co_{0.2}O_2$ phase requires significant involvement from manganese and cobalt (see assumptions and calculations in Table SII and visualization in Fig. S1).

To measure changes in the oxidation state of TMs in the bulk of the material (Fig. 3a), we perform a series of hard XAS measurements at the K-edges of the elements of interest (Ni, Co, Mn). We focus on the XANES spectra, which result from the excitation of the metal 1 s electron to a valence orbital. The quadrupole-allowed pre-edge transitions correspond to the 1s $\rightarrow$ 3d excitations, while the dipole allowed edge transitions consist of 1s $\rightarrow$ 4p excitations. The shapes of the pre-edge and edge peaks are related to the structural environment of the element, while the position of the edge in a XANES spectrum is known to be sensitive to the oxidation state of the element, where a shift to the higher energies corresponds to an oxidation of the element and a shift to the lower energies corresponds to a reduction of the element.[39,41]

Ex situ hard XAS measurements were carried out on harvested cathodes, which were brought to the different lower cut-off potentials of 1.60 V (xLi = 1.20), 1.52 V (xLi = 1.33), 1.03 V (xLi = 1.51), 1.01 V (xLi = 1.68) and 0.8 V (xLi = 2.06). The intercalation/deintercalation profiles for these electrodes can be found in Fig. S2, while the used lower cut-off potentials are highlighted by triangular markers in Fig. 1b. Figure 5 presents the normalized Mn, Co and Ni K-edge XANES spectra of the NMC622 electrodes. Since the peak position at the three studied K-edges shifts to the left throughout the overlithiation process, it is clear that all three TMs participate in the reduction. We estimate the oxidation state of each TM from the spectra of the standards by using a linear relationship between the energy of the edge at the normalized intensity of 0.5 and the oxidation state, as previously reported in literature.[26] The standards used are MnO (Mn^{2+}),[26] Mn_2O_3 (Mn^{3+}),[26] pristine NMC622 (Mn^{4+}, Co^{3+}, $Ni^{2.66+}$), $CoCl_2$ (Co^{2+}) and NiO (Ni^{2+}).

Focusing on the nickel, we can see that the 1.6 V plateau (x in $Li_xNi_{0.6}Mn_{0.2}Co_{0.2}O_2$ = 1.20 and 1.33) is associated with a gradual but small shift toward the lower edge energy and therefore a small change from $Ni^{2.66+}$ oxidation state in the pristine electrode to lower values. As the lithiation degree increases from x = 1.33 to x = 1.51 and the lithiation plateau drops to $\sim$1.0 V, a significant reduction in Ni oxidation state to about $Ni^{2.30+}$ is observed. Further lithiation along the 1.0 V plateau, however, does not lead to an additional shift in the edge energy, indicating that the change in the chemical state should be occurring in either Co or Mn. As the potential drops below 1.0 V and approaches the 0.8 V plateau, another significant change in the Ni edge position occurs, bringing the bulk oxidation state to $Ni^{1.91+}$.

For the cobalt, the K-edge shifts slightly to the left as x in $Li_xNi_{0.6}Mn_{0.2}Co_{0.2}O_2$ increases from 1.00 in the pristine electrode to 1.20 in the first ex situ sample and then remains at approximately the same edge position during additional lithiation along the 1.6 V plateau (x = 1.20 and 1.33 in $Li_xNi_{0.6}Mn_{0.2}Co_{0.2}O_2$). In similarity to Ni, as the lithiation degree increases further from x = 1.33 to x = 1.51 and the lithiation plateau drops to $\sim$1.0 V, a significant decrease in Co oxidation state to approximatively $Co^{2.43+}$ is observed. Further lithiation of NMC622, which increases Li stoichiometry first to x = 1.68 and then to x = 2.06, results in gradual shift in Co edge position to the left and a final lower oxidation state of Co of approximatively $Co^{2.21+}$.

In comparison to Ni and Co K-edges, Mn K-edge shifts only slightly during the first lithiation plateau at 1.6 V, resulting in slightly reduced Mn ($Mn^{3.94+}$). As the stoichiometry of lithium in $Li_xNi_{0.6}Mn_{0.2}Co_{0.2}O_2$ increases from x = 1.33 to x = 1.51, and the potential drops to $\sim$1.0 V, the Mn oxidation decreases significantly,

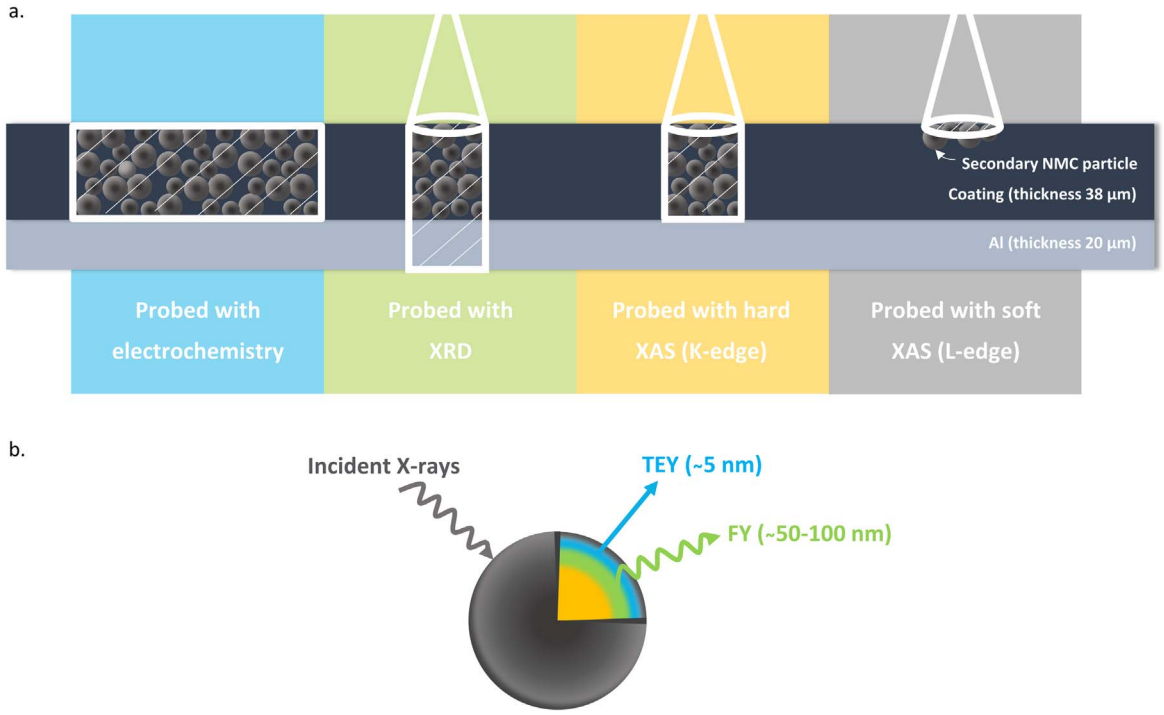

Figure 3. (a) Comparison of the different depths probed by electrochemistry, XRD, hard XAS (K-edge) and soft XAS (L-edge) on an electrode with a coating of thickness 38 μm, aluminum sheet of thickness 20 μm and secondary particles with diameter of 7–10 μm; (b) Depths probed by incident soft X-ray on a single secondary particle.

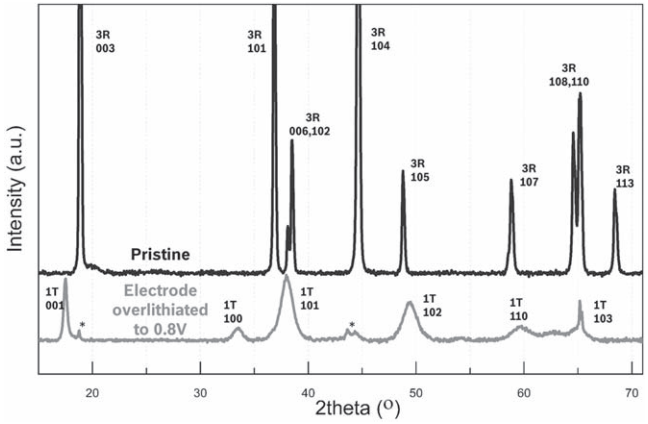

Figure 4. Ex situ X-ray diffraction pattern of $Li_xNi_{0.6}Mn_{0.2}Co_{0.2}O_2$ electrodes (pristine electrode and x = 2.06). The Miller indices of the Bragg peaks are indicated near each peak, 3 R refers to peaks of the $3RLiMO_2$ phase and 1 T refers to the peaks of the $1T\text{-}Li_2NiO_2$ phase, the peaks marked by an asterisk indicate the remaining peaks from the $3R\text{-}LiMO_2$ phase.

going from $Mn^{3.94+}$ to $Mn^{3.02+}$. Further reduction along the 1.0 V plateau leads to a small shift in the Mn K-edge to the left, while the transition to the 0.8 V lithiation plateau results in another significant change in Mn chemical state, bringing Mn to an oxidation state of about $Mn^{2.57+}$.

Using the estimated oxidation states of all three TM oxides, it is possible to calculate the amount of charge that would need to enter the electrode to result in these measured values and compare the calculated capacity to the capacity, which was obtained electrochemically. The results of these calculations are presented in Table SIII. Examination of the values reveals that the capacities calculated from the hard XAS data are in reasonable agreement with the capacities reached by the harvested cathodes, suggesting that contributions to gravimetric capacity from side reactions were minor.

To distinguish between electrochemistry occurring at the surface of the particles and the changes throughout their bulk, hard XAS measurements are followed by soft XAS study, using both Total Electron Yield (TEY) and Fluorescence Yield (FY) modes. The measurements are executed at the L-edge of Ni, Co, and Mn, probing the electron dipole transition from the 2p core level to the 3d valence states.[42] As shown in Fig. 3b, the TEY mode detects the oxidation state of the elements in the top 5–10 nm of the film and the FY mode probes deeper into the bulk of the material (~50–100 nm).[43] The differences in the spectra obtained in TEY mode (surface) and FY mode (subsurface/bulk) or hard XAS (bulk) will provide information on which electrochemical processes are first occurring at the surface of the particles.

Ex situ soft XAS measurements were carried out on harvested cathode electrodes brought to the lower cut-off potentials of 1.60 V (xLi = 1.20), 1.52 V (xLi = 1.33), 1.03 V (xLi = 1.51), 1.01 V (xLi = 1.68) and 0.8 V (xLi = 2.06), as shown in Fig. 1b. The changes in the Ni L-edge, in Figs. 6a and 6b, can be interpreted by comparison of the $L_{3,high}/L_{3,low}$ ratio of the different spectra with standards,[44,45] as presented in Fig. S3. The surface Ni (TEY, Fig. 6a) is much more reduced than the subsurface Ni (FY, Fig. 6b) for the pristine electrode, as was reported for NMC622 in the potential window of 3.0 V to 4.4 V by Tian et al.[16] This gradient in the Ni oxidation state within the particle continues upon deep lithiation. The surface Ni is already reduced to approximatively Ni^{2+} along the first plateau (x = 1.20 and 1.33 in $Li_xNi_{0.6}Mn_{0.2}Co_{0.2}O_2$), while both the subsurface (Fig. 6b) and the bulk of the particles (Fig. 5) remain at a higher oxidation state. The persistence of the gradient in the Ni oxidation state within the particle indicates that the reduction of the Ni initiates at the surface and then propagates toward the bulk.

Focusing on the Co TM, the L-edge spectra shown in Fig. 7 are qualitatively interpreted by comparison with standards (CoO for Co^{2+} and pristine NMC622 for Co^{3+}).[46] By examining the shapes of the TEY and the FY spectra, we can observe that in similarity to Ni there is a difference in the Co oxidation state within the particle. More specifically, a clear reduction of the surface Co can be observed as early as x = 1.20 (Fig. 7a), whereas the subsurface

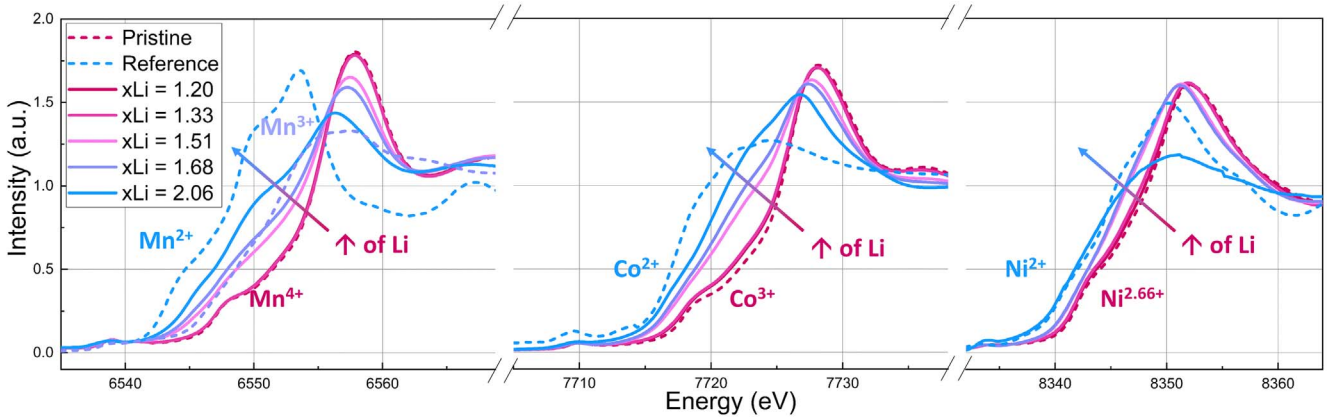

Figure 5. Mn, Co, and Ni K-edge spectra of $LixNi_{0.6}Mn_{0.2}Co_{0.2}O_2$ with x = 1.20, 1.33, 1.51, 1.68 and 2.06. Pristine NMC622 (Mn^{4+}, Co^{3+}, $Ni^{2.66+}$), NiO (Ni^{2+}), $CoCl_2$ (Co^{2+}), MnO (Mn^{2+}),[26] Mn_2O_3 (Mn^{3+})[26] used as standards.

(Fig. 7b), in agreement with the hard XAS data, shows significant reduction of the Co only along the second plateau.

We note that the Co signal for the TEY mode for the electrode lithiated to x = 2.06 in $Li_xNi_{0.6}Mn_{0.2}Co_{0.2}O_2$ was insufficient and is not presented here. Because a similar issue was also observed with the other minor TM component in NMC622 (Mn, Fig. 8), it is likely that the insufficient signal for both Co and Mn occurred due to a combination of an ex situ measurement of a highly lithiated and therefore reactive electrode surface and the low concentration of the element in the sample, as discussed by Johnson et al.[47] Additionally Co, has a satellite peak, which we label as A_2 in its TEY spectra. This peak can be attributed to the metal-to-ligand charge transfer (MLCT) transitions to unoccupied ligand orbitals, which could appear due to carbonated degradation by-products on the surface of the particles, as was previously observed for different Ni and Co systems.[48–50]

Only TEY data is shown for the Mn L-edge XAS spectra (Fig. 8), as the FY signal of the Mn L-edge is distorted by the O-K emissions.[42,51] The L-edge spectra are qualitatively interpreted by comparison with standards (MnO for Mn^{2+} and pristine NMC622 for Mn^{4+}). A small oxidation of the Mn^{2+} standard is observed and results from a minimal contact with air during transfer into the vacuum chamber of the beamline.[42] Similarly to Co, a clear reduction of Mn^{4+} towards Mn^{2+} is observed for x = 1.20 in $Li_xNi_{0.6}Mn_{0.2}Co_{0.2}O_2$ along the first plateau, while the reduction of the bulk Mn observed with the K-edge spectra initiates along the second plateau. As a result, it is possible to conclude that the reduction of Mn also initiates from the surface of the particles and then proceeds into their bulk.

The combination of soft and hard XAS studies establishes a depth-resolved understanding of the reduction of the TMs upon deep overlithiation of NMC622. Along the first plateau (x = 1.20 and 1.33

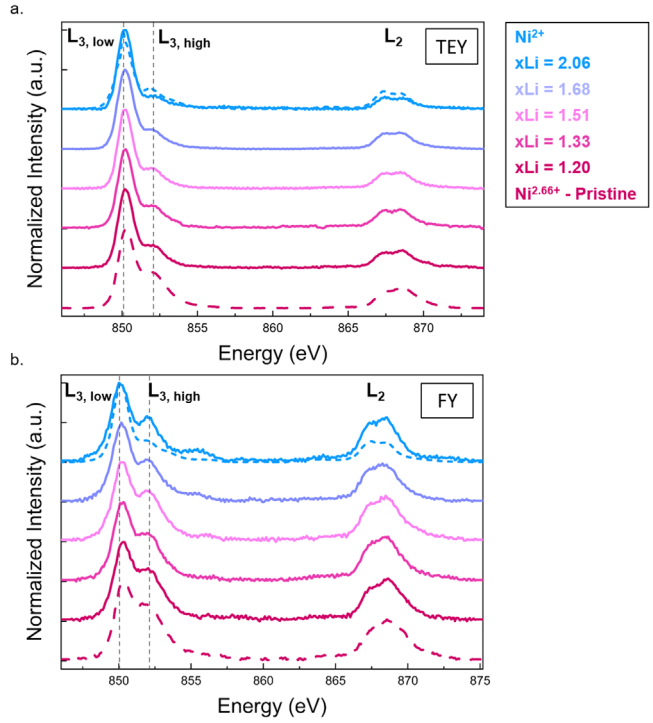

Figure 6. Ni L-edge XAS spectra of $Li_xNi_{0.6}Mn_{0.2}Co_{0.2}O_2$ electrodes with x = 1.20, 1.33, 1.51, 1.68 and 2.06 compared to the pristine material and NiO standard, (a) TEY; (b) FY.

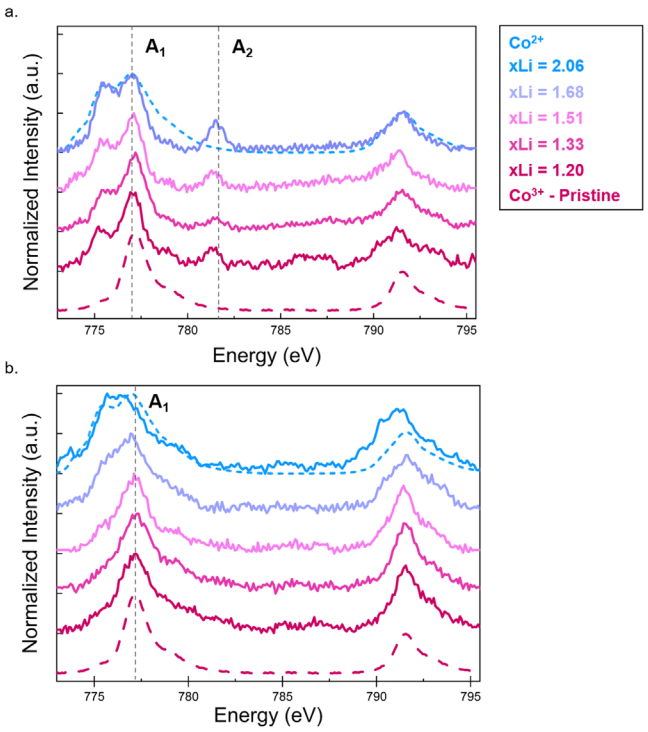

Figure 7. Co L-edge XAS spectra of $Li_xNi_{0.6}Mn_{0.2}Co_{0.2}O_2$ electrodes with x = 1.20, 1.33, 1.51, 1.68 and 2.06 compared to the pristine material and CoO standard; (a) TEY; (b) FY; the characteristic peak position of Co^{3+} is highlighted by the position of A_1, while the peak at the position of A_2 is attributed to a metal-to-ligand charge transfer (MLCT). The TEY absorption spectra for xLi = 2.06 is not shown here, due to insufficient Co signal.

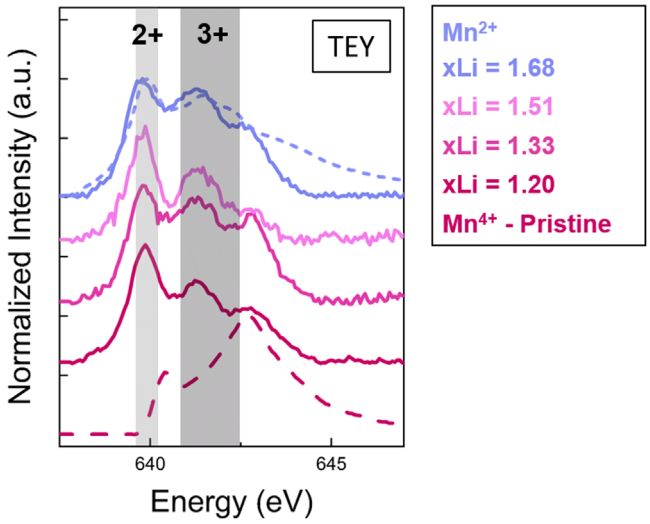

Figure 8. Mn L-edge XAS spectra of $Li_xNi_{0.6}Mn_{0.2}Co_{0.2}O_2$ electrodes with x = 1.20, 1.33, 1.51, 1.68, compared to the pristine material and MnO standard; we note that despite of the precautions taken during sample transfer, a minimal exposure of the samples to air is expected and can be seen from the slight oxidation of the MnO standard, which is particularly sensitive to air. The highlighted areas mark the characteristic peaks of Mn^{2+} and Mn^{3+}. The TEY absorption spectra for xLi = 2.06 is not shown here as the Mn signal was insufficient.

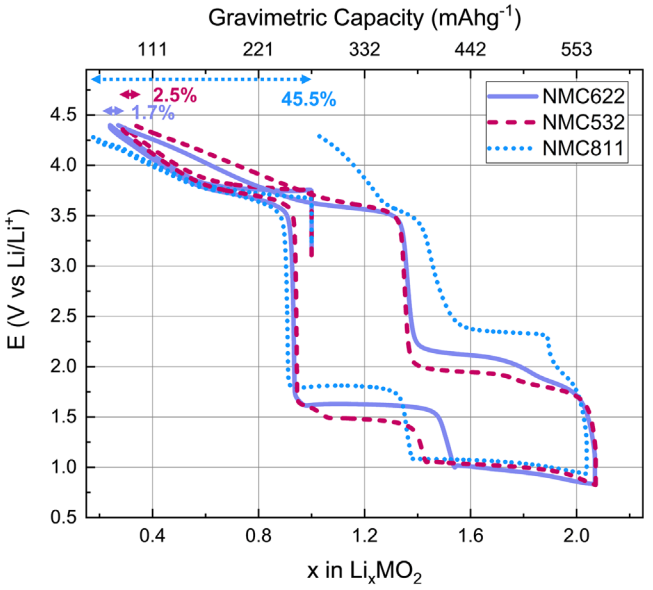

Figure 9. Intercalation/deintercalation profile of Li_xMO_2 (M = Ni, Mn, Co), 1 M $LiPF_6$ in EC-DEC 50:50 half-cells cycled at 0.1C. NMC622 and NMC532 were first delithiated to 4.4 V and NMC811 half-cells was delithiated to 4.3 V to limit side reactions at high voltage, a lithiation to 3.0 V and a delithiation to their respective upper cut-off voltage was run for comparison. All cells were then lithiated to xLi = 2.06 and delithiated to their respective upper voltage cut-off. A loss of capacity of 1.7% for NMC622, 2.8% for NMC532 and 45.5% for NMC811 is observed upon the first overlithiation cycle.

in $Li_xNi_{0.6}Mn_{0.2}Co_{0.2}O_2$), the bulk Ni and Co begin to reduce, while the reduction of bulk Mn is minimal. Additionally, a clear reduction of all TMs is initiated at the surface of the particles at this same state of lithiation. Thus, in contrast with the study of $Li_xNi_{0.5}Mn_{0.5}O_2$ done by Johnson et al.,[47] the gain of capacity along the first plateau is not only due to the reduction of Ni to Ni^{2+} but also involves bulk reduction of Co and surface reduction of Mn. The transition to the second plateau at around 1.0 V (x = 1.51 in $Li_xNi_{0.6}Mn_{0.2}Co_{0.2}O_2$) marks a significant concerted reduction of the bulk oxidation state of all three TMs.

The knowledge gained from the depth-resolved XAS characterization can be used to create a more accurate model of the surface of the cathode particles during battery operation. As the battery is discharged and the cathode is lithiated, the operation of the battery may become limited by the diffusion rate of lithium ion into the material under certain high power conditions. The performed characterization provides information on the nature of the $Li_2Ni_{0.6}Mn_{0.2}Co_{0.2}O_2$ phase, which would form on the surface of the NMC622 particles, and follow up studies (both experimental and computational) can be designed to extract the diffusion coefficient of lithium ion in $Li_xNi_{0.6}Mn_{0.2}Co_{0.2}O_2$, as x varies between the values of 1 and 2.

Although the primary focus of the current study was to understand the overlithiation properties of the NMC622 electrode, a member of NMC family with intermediate Ni-content, additional electrochemical characterization was also performed on NMC532 and NMC811 cathodes to determine if the observed overlithiation properties were unique to NMC622 or universal to NMC family. Comparison of the intercalation/deintercalation curves in Fig. 9 reveals that although all three materials can be lithiated to stoichiometry of x ~ 2 in Li_xMO_2, it is not possible to regain the initial capacity in the case of NMC811. As seen in the Fig. 9, the capacity losses for the three electrodes are 2.8% for NMC532, 1.7% for NMC622, and 45.5% for NMC811. Further comparison between several overlithiation cycles for NMC622 in Fig. S4 demonstrates that initial reversibility of NMC622 cannot be maintained indefinitely. Future work will focus on understanding of the impact of both Ni-content and repeated cycling on overlithiation properties of various stoichiometry of NMC cathodes.

Conclusions

Our study investigates the changes occurring in NMC622 cathode upon overlithiation. First, electrochemical characterization shows that by decreasing the lower cut-off potential it is possible to recover the capacity "lost" during the first cycle and to intercalate more than one lithium ion into the electrode's structure. Then, ex situ XRD experiments identify that the overlithiation leads to a close to full transition to a $Li_2Ni_{0.6}Mn_{0.2}Co_{0.2}O_2$ phase, suggesting only minor contributions from side reactions and necessitating participation from all transition metals in the reduction process. Building upon XRD results, hard XAS spectra confirm that all three metals, Ni, Co, and Mn, are electrochemically active, reaching oxidation states of approximately $Ni^{2.0+}$, $Co^{2.2+}$, and $Mn^{2.6+}$ at the lowest tested potential. Then, soft XAS spectra demonstrate that the reduction initiates from the surface of the particles, with all three metals consistently showing a lower oxidation state at the surface than in the bulk. The identified properties of bulk $Li_2Ni_{0.6}Mn_{0.2}Co_{0.2}O_2$ phase can be used to create a more accurate model of the surface of the cathode particles during battery operation under high power conditions, during which the surface content of lithium ion could approach the value of 2.

Acknowledgments

The synchrotron X-ray absorption spectroscopy portions of this research were carried out at the Stanford Synchrotron Radiation Lightsource, a Directorate of SLAC National Accelerator Laboratory and an Office of Science User Facility operated for the U.S. Department of Energy Office of Science by Stanford University. Use of the Stanford Synchrotron Radiation Lightsource, SLAC National Accelerator Laboratory, is supported by the U.S. Department of Energy, Office of Science, Office of Basic Energy Sciences under Contract No. DE-AC02-76SF00515. The electrodes were produced at the U.S. Department of Energy's (DOE) CAMP (Cell Analysis, Modeling and Prototyping) Facility, Argonne National Laboratory. The CAMP Facility is fully supported by the DOE Vehicle Technologies Program (VTP) within the core funding

of the Applied Battery Research (ABR) for Transportation Program. The authors would like to acknowledge Bryant J. Polzin for his continued support in quickly providing electrode materials from CAMP.

ORCID

Camille Usubelli https://orcid.org/0000-0001-6350-2364
Münir M. Besli https://orcid.org/0000-0002-0412-0814
Saravanan Kuppan https://orcid.org/0000-0003-4976-4514
Michael Metzger https://orcid.org/0000-0002-5512-8541
Jake Christensen https://orcid.org/0000-0002-3188-6671
Yelena Gorlin https://orcid.org/0000-0002-9242-8914

References

1. S. Aryal, E. V. Timofeeva, and C. U. Segre, *J. Electrochem. Soc.*, **165**, A71 (2018).
2. I. Buchberger, S. Seidlmayer, A. Pokharel, M. Piana, J. Hattendorff, P. Kudejova, R. Gilles, and H. A. Gasteiger, *J. Electrochem. Soc.*, **162**, A2737 (2015).
3. K. Mizushima, P. C. Jones, P. J. Wiseman, and J. B. Goodenough, *Mater. Res. Bull.*, **15**, 783 (1980).
4. E. J. Cairns and P. Albertus, *Annu. Rev. Chem. Biomol. Eng.*, **1**, 299 (2010).
5. P. Y. Liao, J. G. Duh, and S. R. Sheen, *J. Power Sources*, **143**, 212 (2005).
6. H. Arai, S. Okada, Y. Sakurai, and J. Yamaki, *Solid State Ionics*, **95**, 275 (1997).
7. W. Li, J. Reimers, and J. Dahn, *Solid State Ionics*, **67**, 123 (1993).
8. Y.-K. Sun, M. G. Kim, S.-H. Kang, and K. Amine, *J. Mater. Chem.*, **13**, 319 (2003).
9. N. Nitta, F. Wu, J. T. Lee, and G. Yushin, *Mater. Today*, **18**, 252 (2015).
10. N. Yabuuchi, Y. Makimura, and T. Ohzuku, *J. Electrochem. Soc.*, **154**, A314 (2007).
11. I. Belharouak, Y. K. Sun, J. Liu, and K. Amine, *J. Power Sources*, **123**, 247 (2003).
12. K. M. Shaju, G. V. Subba Rao, and B. V. R. Chowdari, *Electrochim. Acta*, **48**, 145 (2002).
13. R. V. Chebiam, F. Prado, and A. Manthiram, *Chem. Mater.*, **13**, 2951 (2001).
14. C. S. Yoon, K. J. Park, U. H. Kim, K. H. Kang, H. H. Ryu, and Y. K. Sun, *Chem. Mater.*, **29**, 10436 (2017).
15. Q. Wang, C. H. Shen, S. Y. Shen, Y. F. Xu, C. G. Shi, L. Huang, J. T. Li, and S. G. Sun, *ACS Appl. Mater. Interfaces*, **9**, 24731 (2017).
16. C. Tian, D. Nordlund, H. L. Xin, Y. Xu, Y. Liu, D. Sokaras, F. Lin, and M. M. Doeff, *J. Electrochem. Soc.*, **165**, A696 (2018).
17. S. T. Myung, F. Maglia, K. J. Park, C. S. Yoon, P. Lamp, S. J. Kim, and Y. K. Sun, *ACS Energy Lett.*, **2**, 196 (2017).
18. N. Zhang, J. Li, H. Li, A. Liu, Q. Huang, L. Ma, Y. Li, and J. R. Dahn, *Chem. Mater.*, **30**, 8852 (2018).
19. K. Märker, P. J. Reeves, C. Xu, K. J. Griffith, and C. P. Grey, *Chem. Mater.*, **31**, 2545 (2019).
20. C. Shen, D. Xiong, L. D. Ellis, K. L. Gering, L. Huang, and J. R. Dahn, *J. Electrochem. Soc.*, **164**, A3349 (2017).
21. H. J. Noh, S. Youn, C. S. Yoon, and Y. K. Sun, *J. Power Sources*, **233**, 121 (2013).
22. C. S. Johnson, J. S. Kim, A. Jeremy Kropf, A. J. Kahaian, J. T. Vaughey, and M. M. Thackeray, *Electrochem. Commun.*, **4**, 492 (2002).
23. J. R. Dahn, U. von Sacken, and C. A. Michal, *Solid State Ionics*, **44**, 87 (1990).
24. S.-H. Kang, S.-H. Park, C. S. Johnson, and K. Amine, *J. Electrochem. Soc.*, **154**, A268 (2007).
25. V. A. Solé, E. Papillon, M. Cotte, P. Walter, and J. Susini, *Spectrochim. Acta - Part B At. Spectrosc.*, **62**, 63 (2007).
26. A. Manceau, M. A. Marcus, and S. Grangeon, *Am. Mineral.*, **97**, 816 (2012).
27. S. M. Webb, *Phys. Scr.*, **2005**, 1011-1015 (2005).
28. R. S. Arumugam, L. Ma, J. Li, X. Xia, J. M. Paulsen, and J. R. Dahn, *J. Electrochem. Soc.*, **163**, A2531 (2016).
29. Y. Ruan, X. Song, Y. Fu, C. Song, and V. Battaglia, *J. Power Sources*, **400**, 539 (2018).
30. J. Choi and A. Manthiram, *Electrochem. Solid State Lett.*, **8**, C102 (2005).
31. J. R. Mueller-Neuhaus, R. A. Dunlap, and J. R. Dahn, *J. Electrochem. Soc.*, **147**, 3598 (2000).
32. Y. M. Todorov and K. Numata, *Electrochim. Acta*, **50**, 495 (2004).
33. R. Weber, C. R. Fell, J. R. Dahn, and S. Hy, *J. Electrochem. Soc.*, **164**, A2992 (2017).
34. S. H. Kang, W. S. Yoon, K. W. Nam, X. Q. Yang, and D. P. Abraham, *J. Mater. Sci.*, **43**, 4701 (2008).
35. J. Li, R. Petibon, S. Glazier, N. Sharma, W. K. Pang, V. K. Peterson, and J. R. Dahn, *Electrochim. Acta*, **180**, 234 (2015).
36. J. Li, L. E. Downie, L. Ma, W. Qiu, and J. R. Dahn, *J. Electrochem. Soc.*, **162**, A1401 (2015).
37. S. H. Kang, D. P. Abraham, W. S. Yoon, K. W. Nam, and X. Q. Yang, *Electrochim. Acta*, **54**, 684 (2008).
38. C. Liu, Z. G. Neale, and G. Cao, *Mater. Today*, **19**, 109 (2016).
39. X. Yu, Y. Lyu, L. Gu, H. Wu, S. M. Bak, Y. Zhou, K. Amine, S. N. Ehrlich, H. Li, K. W. Nam, and X. Q. Yang, *Adv. Energy Mater.*, **4**, 1 (2014).
40. R. Benedek, J. Vaughey, and M. M. Thackeray, *Chem. Mater.*, **18**, 1296 (2006).
41. M. L. Baker, M. W. Mara, J. J. Yan, K. O. Hodgson, B. Hedman, and E. I. Solomon, *Coord. Chem. Rev.*, **345**, 182 (2017).
42. R. Qiao, T. Chin, S. J. Harris, S. Yan, and W. Yang, *Curr. Appl Phys.*, **13**, 544 (2013).
43. J. Stohr, *NEXAFS Spectroscopy* (Springer, Berlin Heidelberg)Editor (1992).
44. M. M. Besli et al., *J. Mater. Chem. A*, **7**, 12593 (2019).
45. F. Lin, I. M. Markus, D. Nordlund, T. C. Weng, M. D. Asta, H. L. Xin, and M. M. Doeff, *Nat. Commun.*, **5**, 3529 (2014).
46. F. M. F. De Groot, M. Abbate, J. Van Elp, G. A. Sawatzky, Y. J. Ma, C. T. Chen, and F. Sette, *J. Phys. Condens. Matter*, **5**, 2277 (1993).
47. C. S. Johnson, J. S. Kim, A. J. Kropf, A. J. Kahaian, J. T. Vaughey, L. M. L. Fransson, K. Edström, and M. M. Thackeray, *Chem. Mater.*, **15**, 2313 (2003).
48. T. Hatsui, Y. Takata, and N. Kosugi, *Chem. Phys. Lett.*, **284**, 320 (1998).
49. Y. Takata, T. Hatsui, and N. Kosugi, *J. Electron Spectros. Relat. Phenomena*, **101–103**, 443 (1999).
50. H. Liu et al., *Nano Lett.*, **7**, 1919 (2007).
51. D. Asakura et al., *AIP Adv.*, **6**, 1 (2016).